ELSEVIER

Journal of Nuclear Materials 241–243 (1997) 149–166

journal of nuclear materials

Experimental investigation of transport phenomena in the scrape-off layer and divertor

B. LaBombard [a,*], J.A. Goetz [a], I. Hutchinson [a], D. Jablonski [a], J. Kesner [a], C. Kurz [a,1],
B. Lipschultz [a], G.M. McCracken [a], A. Niemczewski [a,2], J. Terry [a], A. Allen [a],
R.L. Boivin [a], F. Bombarda [b], P. Bonoli [a], C. Christensen [a], C. Fiore [a], D. Garnier [a],
S. Golovato [a,3], R. Granetz [a], M. Greenwald [a], S. Horne [a,4], A. Hubbard [a], J. Irby [a], D. Lo [a],
D. Lumma [a], E. Marmar [a], M. May [c], A. Mazurenko [a], R. Nachtrieb [a], H. Ohkawa [a],
P. O'Shea [a], M. Porkolab [a], J. Reardon [a], J. Rice [a], J. Rost [a], J. Schachter [a], J. Snipes [a],
J. Sorci [a], P. Stek [a], Y. Takase [a], Y. Wang [a], R. Watterson [a,5], J. Weaver [d], B. Welch [d],
S. Wolfe [a]

[a] *Plasma Fusion Center, Massachusetts Institute of Technology, Cambridge, MA, USA*
[b] *Associazione Euratom-ENEA sulla Fusione, Frascati, Italy*
[c] *Johns Hopkins University, Baltimore, MD, USA*
[d] *University of Maryland, College Park, MD, USA*

Abstract

Transport physics in the divertor and scrape-off layer of Alcator C-Mod is investigated for a wide range of plasma conditions. Parallel (||) transport topics include: low recycling, high-recycling, and detached regimes, thermoelectric currents, asymmetric heat fluxes driven by thermoelectric currents, and reversed divertor flows. Perpendicular ($\perp$) transport topics include: expected and measured scalings of $\perp$ gradients with local conditions, estimated $\chi_\perp$ profiles and scalings, divertor neutral retention effects, and L-mode/H-mode effects. Key results are: (i) classical || transport is obeyed with ion–neutral momentum coupling effects, (ii) $\perp$ heat transport is proportional to local gradients, (iii) $\chi_\perp \propto T_e^{-0.6}\ n^{-0.6}\ L^{-0.7}$ in L-mode, insensitive to toroidal field, (iv) $\chi_\perp$ is dependent on divertor neutral retention, (v) H-mode transport barrier effects partially extend inside the SOL, (vi) inside/outside divertor asymmetries may be caused by a thermoelectric instability, and (vii) reversed || flows depend on divertor asymmetries and their implicit ionization source imbalances.

Keywords: Alcator C-mod; Sol plasma; Transverse transport; Scaling law

1. Introduction

Accurate, physics-based models of cross-field transport in both the core and scrape-off layer (SOL) plasma regions continue to remain elusive, despite considerable effort by the fusion research community. The core plasma exhibits a rich set of transport phenomenology including *L*/*H* confinement modes [1], PEP modes [2,3] and ERS/NCS modes [4,5]. It is believed that sheared poloidal plasma flows may play a role in regulating and reducing the

---

[*] Corresponding author. Tel.: +1-617 253 7264; fax: +1-617 253 0627; e-mail: labombard@cmod2.pfc.mit.edu.

[1] Present address: University of California, San Diego, CA, USA.

[2] Present address: McKinsey and Company, Inc., London, UK.

[3] Present address: Tokyo Electron America, Beverly, MA, USA.

[4] Present address: Applied Science and Technology, Inc., Woburn, MA, USA.

[5] Present address: CPClare Corporation, Lexington, MA, USA.

PII S0022-3115(96)00502-8

turbulence-induced cross-field transport in some enhanced confinement regimes.

In the divertor and SOL plasma regions, it has often been assumed that the description of the cross-field transport mechanisms is much simpler, perhaps being described by a Bohm diffusion coefficient, for example. However, it has become clear that even in the SOL plasma, a much more complicated description is required. For example, H-mode plasmas exhibit increased perpendicular pressure gradients relative to L-mode not only just inside the last closed flux surface (LCFS) but also *outside* the LCFS, extending partly into the SOL. From the practical point of view of estimating the SOL and divertor conditions in a full-scale fusion reactor, one therefore must consider the relevant *core plasma* confinement regime. These observations also imply something about the underlying transport physics: the H-mode transport barrier may be intrinsically linked to conditions in the SOL, extend into the SOL, or even be initially formed in the SOL plasma.

An additional complication that must be faced in transport descriptions of the divertor/SOL is the inside/outside divertor temperature and density asymmetries which depend on the direction of the toroidal magnetic field [6]. Poloidally asymmetric cross-field transport resulting from classical drifts, anomalous transport, and/or toroidal effects may play a role in the inside/outside asymmetry by providing unbalanced heat and/or particle exhaust. Once a heat flux asymmetry exists, divertor radiation can amplify the asymmetry and regulate the heat flux arriving at the divertor plates. However, cross-field transport is not the only mechanism which can produce a heat flux asymmetry. It has been pointed out that asymmetric, *parallel* heat transport might also exist in the SOL, driven by thermoelectric currents [7,8]. Over a well defined collisionality range, an instability mechanism can occur: inside/outside electron temperature differences can drive thermoelectric currents which in turn result in asymmetric parallel heat transport.

Reversed parallel particle flows in the divertor have been predicted by both basic theoretical considerations (for example Ref. [9]) and 2D fluid codes, and have been measured on some tokamaks [10,11]. Reversed flows can potentially influence the impurity retention characteristics of a divertor, providing a mechanism for divertor impurities to be transported into the main plasma chamber. It is therefore important to characterize the conditions under which flow reversal occurs and to develop a working understanding of the underlying causes.

Edge-plasma measurements in experimental tokamaks are becoming sufficiently detailed to begin building a picture of divertor/SOL transport phenomena based on empirical dependencies and to test some simple physics-based transport hypotheses. On Alcator C-Mod, [12] extensive divertor/SOL diagnostics [13] have yielded a rich set of observations in this area. This paper reports on some recent results, focusing on single-null, L-mode discharges over a wide range of core plasma densities, toroidal magnetic fields, and plasma currents. Data from a smaller set of H-mode discharges are presented and compared to L-mode results.

Section 2 describes the divertor geometry and arrangement of diagnostics. Most of the results presented in this paper were obtained from Alcator C-Mod's Langmuir probe systems. These systems are consequently discussed in some detail. Measurements of cross-field profiles in the SOL and divertor plasma are presented in Section 3. Plasma conditions leading to formation of temperature gradients along field lines, plasma detachment, and the occurrence of a related phenomenon, termed the divertor 'death-ray', are discussed. Experimental evidence of strong plasma–neutral momentum coupling based on these and other observations is presented. In Section 4, expected scalings of heat transport in the divertor and scrape-off layer are discussed with the help of a simplified heat transport model. The scaling of measured cross-field gradients with local electron temperature, density, connection length and toroidal field strength is investigated in detail by means of regression analysis in Section 5. Radial profiles of cross-field heat diffusivity for L- and H-mode plasmas are estimated in Section 6. Section 7 describes observations of inside/outside divertor asymmetries and their dependence on the edge plasma collisionality and toroidal field direction. Thermoelectric currents and their potential role in causing and/or maintaining a parallel heat flux asymmetry are also investigated. Finally, the conditions which lead to reversed parallel flows in the divertor are reported. Section 8 summarizes the key results of this work.

2. Experimental arrangement

All results reported in this paper were obtained in deuterium discharges with the magnetic equilibrium in the divertor similar to that of Fig. 1. All discharges had I_p parallel to B_T and, with the exception of some discharges discussed in Section 7, had the $B \times \nabla B$ ion drift directed towards the lower x-point. The geometry of the divertor and the arrangement of divertor probe diagnostics is shown in Fig. 1. Detailed information on Alcator C-Mod's design, diagnostics, and operational characteristics can be found elsewhere [12].

Langmuir probes are mounted on both the inner and outer divertor plates at 16 poloidal locations. Before July 1995, molybdenum probes were used, extending 0.5 mm beyond the surface of the divertor and presenting a 'domed' surface to the plasma flux. Tungsten probe replacements were installed by October 1995, also extending 0.5 mm beyond the surface but having a fixed, 10° angle with respect to the divertor surface. These geometries avoid problems associated with the interpretation of probe characteristics at small oblique field line angles [14]. Plasma

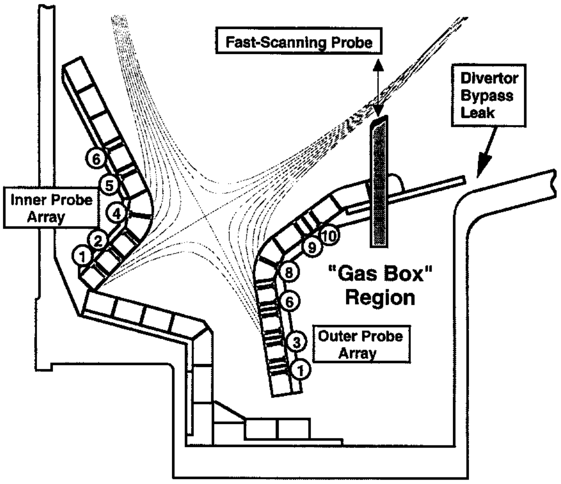

Fig. 1. Cross-section of Alcator C-Mod showing divertor geometry, divertor probe diagnostics and a typical plasma equilibrium used for these studies. A neutral gas leakage path (bypass) connecting between the volume behind the outer divertor (gas box) and the main plasma chamber was closed during the 1995 summer maintenance period.

density and temperature profiles across the divertor surface are deduced at roughly 10 ms intervals by fitting current–voltage characteristics using standard magnetized probe theory [15].

A fast-scanning Langmuir probe is used to record SOL plasma profiles up to the last closed flux surface at a position 'upstream' from the entrance to the outer divertor. The probe head consists of a 15 mm diameter molybdenum body with four Langmuir probe elements (molybdenum before July 1995, tungsten after). The probe elements have directional sensitivity (along and across B), maintain a field line grazing angle of about 20°, and project a current-collecting area with dimension transverse to flux surfaces of 0.5 mm mapped to the midplane. Densities and temperatures along the probe's trajectory are obtained every 0.33 ms (corresponding to 0.3 mm of vertical probe travel) by fitting positive and negative-going I–V characteristics generated by a 1500 Hz voltage sweep. (A 500 Hz sweep was used before March 1995.)

Data from the divertor probe array and the fast-scanning probe are mapped onto magnetic flux surfaces reconstructed from magnetic measurements [16] and the EFIT plasma equilibrium code [17]. Flux surfaces in the scrape-off layer are labeled by the coordinate ρ, which is defined as the distance in major radius outside the last-closed flux surface at the outboard mid-plane. The electron stagnation pressure profiles measured by the divertor and scanning probes can be made to overlay by adjusting their relative flux surface mappings by 0–2 mm in ρ. This level of mapping error is within the expected accuracy of the EFIT reconstruction and the positioning accuracy of the scanning probe. The results and analysis presented in this paper are insensitive to mapping errors of this magnitude.

Before July 1995, a toroidally continuous gas leakage pathway existed between the outer divertor 'gas box' and the main plasma chamber (shown in Fig. 1). Experiments determined that the neutral leakage flux through this opening (bypass) was a significant fraction of the total particle recycling fluxes [18], causing a reduction in the ratio of divertor to midplane neutral pressures (compression ratio). The bypass was closed during the 1995 summer maintenance period, resulting in an increase in compression ratios from 70 (before July 1995) to 250 (after October 1995) for similar discharges.

Beginning in January 1996, boronization of Alcator C-Mod's molybdenum and stainless steel first wall and vacuum wall surfaces was performed. A mixture of 90% helium and 10% diborane was substituted for the fill gas in the electron–cyclotron discharge cleaning (ECDC) plasmas. This boronization procedure resulted in a significantly improved core plasma performance: reproducible high-confinement H-mode plasmas (H-factors up to ~ 2.5), reduction in intrinsic carbon and oxygen impurities, factor of ~ 2 of more reduction in molybdenum impurity levels, lower core plasma radiation, and higher power levels in the SOL (≥ 2 MW).

3. SOL and divertor observations

3.1. Parallel temperature and pressure gradients

Fig. 2 compares the SOL plasma profiles measured by the outer divertor probe array and the fast-scanning probe. Electron stagnation pressure and temperature profiles are shown for four values of central line-averaged density in otherwise similar discharges ($I_p = 0.8$ MA, $B_T = 5.3$ T, boronized walls, ohmic L-mode). The curves labeled as 'upstream' in Fig. 2 result from smooth spline fits to temperature and density data points from a single in- and out-going scan of the four Langmuir probe elements on the scanning probe (~ 400 data points). The 'downstream' data points are each from a 40 ms time average of a divertor probe's data output (~ 4 data points). Note that electron stagnation pressure is defined as $nT_e(1 + M^2)$, corresponding to nT_e for the 'upstream' data points (parallel Mach number, $M < 0.3$) and $2nT_e$ for the datapoints at the divertor (or probe) sheath edge ($M = 1$).

Two regimes of parallel plasma transport to the divertor surface are identified in Fig. 2(a) that depend on the core density:

(1) Profiles at low density, $\bar{n}_e \lesssim 1.4 \times 10^{20}$ m^{-3}, exhibit an electron temperature that falls by less than ~ 30% along the magnetic field lines. Electron pressure is constant along B and the divertor sheath supports most of the

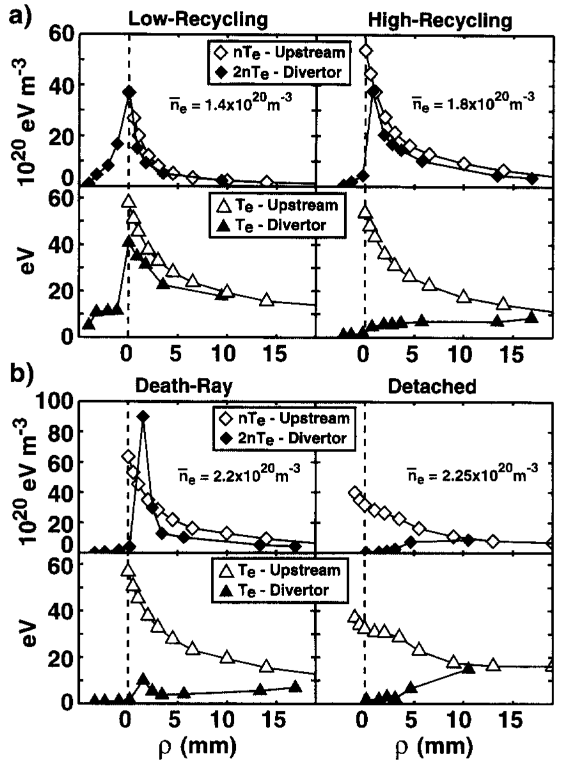

Fig. 2. Comparison of electron temperature and pressure profiles 'upstream' and at the divertor plate for four values of line-averaged density. (a) 'low-recycling' (small parallel T_e gradients) and 'high recycling' (large parallel T_e gradients) regimes are evident at low and medium densities. (b) Divertor 'detachment' (large parallel nT_e gradients) occurs at the highest densities. A transition regime, dubbed the 'death-ray', is sometimes observed at core densities just below the detachment threshold.

temperature drop. This regime is often referred to as the 'low recycling' or 'sheath-limited' heat transport regime. Electron temperatures everywhere in the SOL are the hottest in this low density regime.

(2) Profiles at moderate density, $\bar{n}_e \sim 1.8 \times 10^{20}$ m^{-3}, show a 'high recycling' divertor condition across the profile: the electron temperature falls at the divertor plate relative to 'upstream' while the density rises so as to keep pressure approximately constant along *B*.

Fig. 2(b) displays two other regimes of parallel plasma transport to the divertor surface that occur in the high density range ($\bar{n}_e > 2.1 \times 10^{20}$ m^{-3}):

(3) At high densities, a 'detached' plasma condition extends from the separatrix out to $\rho \sim 5$ mm Both the divertor electron temperature *and* the density are very much lower than the upstream values in this regime, violating constant pressure along *B*.

(4) At plasma densities just below the detachment threshold, a transition regime, dubbed the 'death-ray', is often observed. Electron pressures at the divertor plate exceed upstream values by a factor of 2 or more over a narrow region ($\Delta\rho = 1$–2 mm) of the divertor profile. Elsewhere across the divertor plate, the electron pressure is lower than upstream, implying a redistribution and focusing of parallel plasma momentum into the narrow 'death-ray' region.

Detached, high-recycling, and low-recycling (sheath-limited) regimes often coexist across the SOL profile in the same discharge. Electron temperature profiles at the outer divertor plate generally show an inverted profile (T_e increasing with ρ) in discharges where a high-recycling or detached regime appears near the separatrix.

Fig. 3 shows an example of this trend and illustrates the role of parallel electron collisionality and volumetric power losses (radiation) in determining the inverted temperature profile. Near the separatrix, the ratio of upstream/plate electron temperature is around 10 and the local divertor density peaks at a value that is ~ 2 times the upstream density. The divertor electron stagnation pressure at the separatrix is $\sim 1/2$ the upstream value, indicating a high-recycling/detached regime. For $\rho \gtrsim 8$ mm, the electron temperature ratio approaches unity and the density is ~ 0.5 times the upstream value (low-recycling regime). The ratio

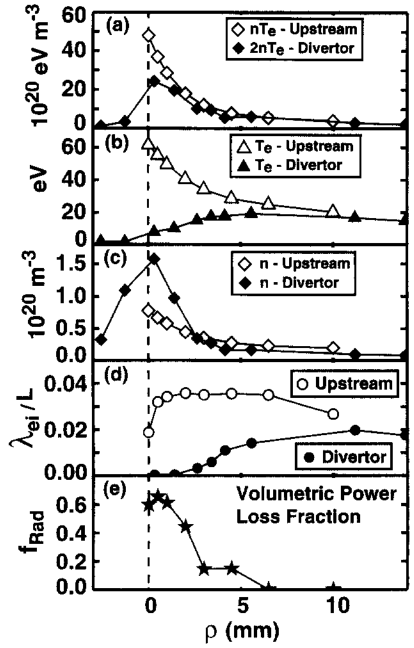

Fig. 3. Upstream and downstream profiles of electron pressure, temperature, density, and ratio of electron–ion mean free path normalized to 1/2 the total connection length (λ_{ei}/L). An estimate of f_{Rad} (radiated/total power) from local power balance suggests that the high density and resultant radiation near the strike point region is the principal cause of parallel temperature gradients to be the largest at that location.

of parallel electron mean free path [19] [6] normalized to 1/2 the magnetic connection length (λ_{ei}/L) is plotted in Fig. 3(d) for upstream and divertor plate conditions. Fig. 3(e) shows an estimate of f_{Rad} deduced from profile measurements where ($1 - f_{Rad}$) is the parallel heat flux at the divertor surface normalized to the upstream heat flux arising from electron conduction. (f_{Rad} is precisely defined in Section 4.1) This quantity estimates the fraction of the total power on a flux surface that is dissipated via volumetric losses in the divertor. For flux surfaces near the separatrix, these volumetric losses include power flow into the private flux zone.

Although the upstream/plate electron temperature ratio changes by an order of magnitude across the SOL profile, the upstream collisionality remains essentially constant across the profile. (The drop in λ_{ei}/L near the separatrix is caused by the sharp increase in the value of L as the x-point is approached.) The transition from high- to low-recycling is therefore not simply explained by a spatial variation in the upstream collisionality. On the other hand, the volumetric losses (f_{rad}) show a strong variation across the SOL profile, generally following the divertor density profile and peaking near the separatrix. One would expect f_{rad} to be approximately proportional to the local divertor density for the case of a constant impurity fraction. Thus, the transition from detached/high-recycling to low-recycling regime across the profile is consistent with a variation in the volumetric losses across the profile caused by both radiation and losses into the private flux zone. $\lambda_{ei}/L \ll 1$ is a necessary condition for the formation of parallel temperature gradients. However, the magnitude of the resulting gradient is apparently determined by the local power balance.

Divertor detachment is observed when the electron temperature at the divertor plate falls below ~ 5 eV. Fig. 4 shows plasma conditions at $\rho = 2$ mm on the outer divertor surface for a series of nearly identical discharges in which the core plasma density was varied. Above 10 eV, the ratio of upstream to downstream electron stagnation pressures remains constant at around ~ 1. In the range when $T_e = 5$–10 eV a divertor 'death-ray' is sometimes seen. As shown previously in Fig. 2(b), this phenomenon appears as a highly localized increase in the electron stagnation pressure that exceeds the upstream value by a factor of 2 or more. Excluding 'death-ray' points, the pressure ratio maintains a value of ~ 1 down to electron temperatures of ~ 5 eV. Below ~ 5 eV, divertor electron pressure falls as a monotonic function of electron temperature. Accompanying the electron pressure loss is a factor of ~ 50 reduction in the parallel heat flux on the divertor surface.

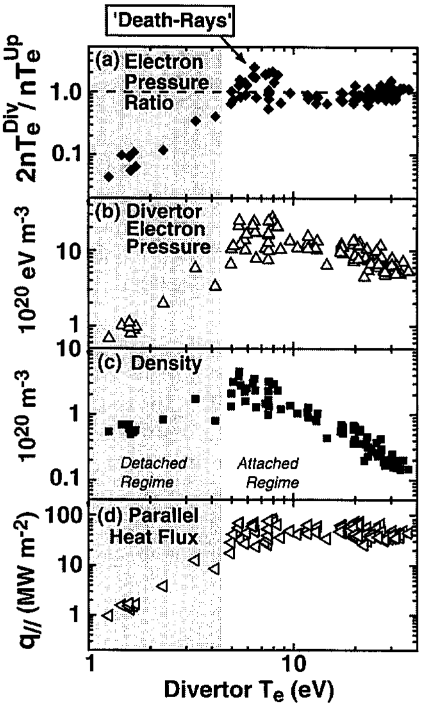

Fig. 4. Outer divertor conditions on the $\rho = 2$ mm flux versus electron temperature at the outer divertor surface: (a) upstream/divertor electron pressure ratio, (b) divertor electron pressure, (c) divertor density, (d) parallel heat flux at divertor surface, inferred from sheath theory with $\gamma = 7$.

The clear correlation between local electron temperature and plasma pressure loss at $T_e \lesssim 5$ eV is strong evidence for ion–neutral collisions being primarily responsible for removing parallel plasma momentum. This picture of momentum loss, originally proposed by Stangeby [20], has remained the most reasonable explanation for detachment phenomena in tokamaks. Recent work with 2D fluid codes [21] suggests that three-body recombination can play a supporting role in reducing the plasma pressure at the divertor plate. Recombination via ion–molecule interactions has also been identified [22,23] as a potentially important process. However, these recombination mechanisms become dominant at low electron temperatures ($T_e \lesssim 2$ eV), well below temperatures in which a significant pressure loss is observed.

In order to remove parallel momentum via ion–neutral collisions, a sufficient density of neutrals must exist in the detachment zone. Neutral density measurements on Alcator C-Mod made both indirectly via pressure gauges [24] and directly from tomographic reconstructions of D_α emission [25] clearly show that a sufficient neutral density exists within the detached plasma to remove the parallel momentum. In fact, assuming that each charge-exchange and elastic scattering event results in 100% loss of parallel ion momentum (neutrals at rest in the laboratory frame),

---

[6] We have used the following definition for the electron–ion mean free path: λ_{ei} (m) $= 1.45 \times 10^{-3}$ $(T_e/\mathrm{eV})^2$ $(n/10^{20}\ \mathrm{m}^{-3})^{-1}$ $(\ln \Lambda)^{-1}$.

then a factor of 10 *too much* momentum loss would be estimated in most cases! Apparently, the scattered neutrals do not communicate directly with the divertor/wall surfaces but rather contribute to a neutral population that acquires toroidal momentum. This scenario is consistent with charge exchange mean free paths (~ 0.8 cm) being smaller than the poloidal width of the divertor fan. In order to reconcile the momentum transfer rate with the neutral density measurements, the neutral 'fluid' must acquire a toroidal velocity that approaches 90% of the plasma flow speed [25,26].

This picture of a toroidally flowing neutral fluid also offers a possible explanation for the divertor 'death-ray' phenomenon. As shown in Fig. 2(b) and Fig. 4(a), (c), the 'death-ray' is a spatially localized ($\Delta\rho = 1$–2 mm), high density zone of plasma at the divertor plate with an electron stagnation pressure that exceeds the upstream value by a factor of 2 or more. Steady-state death-rays have been produced by maintaining divertor conditions near the detachment threshold. These death-rays persist with about the same magnitude at the same flux surface coordinate ($\rho = \sim 2$ mm), despite a sweep of the strike point ($\Delta\rho > 6$ mm) across the divertor surface. The electron temperature in the death-ray is always higher than in surrounding plasma and greater than ~ 6 eV with typical values of 8 to 10 eV. As shown in Fig. 2(b), the surrounding plasma has pressure loss, with plasma on the private flux side being fully detached. Based on the premise that neutrals acquire toroidal momentum in the surrounding, detached plasma regions, one would expect a net parallel momentum *source* to occur in the hotter, death-ray region as these neutrals become ionized and deposit momentum there. Thus, it appears that ion–neutral collisions may provide a mechanism not only to remove parallel momentum from the divertor plasma but also to redistribute parallel momentum across flux surfaces in the divertor.

3.2. *Cross-field temperature and density profiles*

Fig. 5 displays representative cross-field profiles of density, temperature, and electron pressure for three ohmic, L-mode discharges with $\bar{n}_e = 1.3$, 1.9, 2.5×10^{20} m^{-3}, and one ELM-free H-mode discharge with $\bar{n}_e = 3.0 \times 10^{20}$ m^{-3}. All four discharges had similar magnetic equilibria (1.0 MA, 5.3 T). Data from the H-mode discharge were taken immediately after a 2 MW RF heating pulse while the plasma remained in H-mode. This technique was routinely used to avoid the possibility of the probe data being corrupted by RF-sheath rectification effects.

A number of observations can be made: (1) All profiles display a non-exponential dependence on flux surface coordinate, i.e., the slope on the logarithmic plot varies substantially with ρ. For electron pressure, the local gradient scale length can vary by a factor of ~ 4 in L-mode plasmas (~ 2 mm at $\rho = 0$ to ~ 8 mm at $\rho = 15$ mm). (2) Local gradient scale lengths in L-mode plasmas appear to depend on core plasma density, having the smallest values at low density and largest values at high density. (3) Despite the higher core density, H-mode plasmas have a very short pressure gradient scale length at the separatrix with over a factor of 10 variation across the profile (~ 1 mm at $\rho = 0$ to ~ 14 mm at $\rho = 15$ mm).

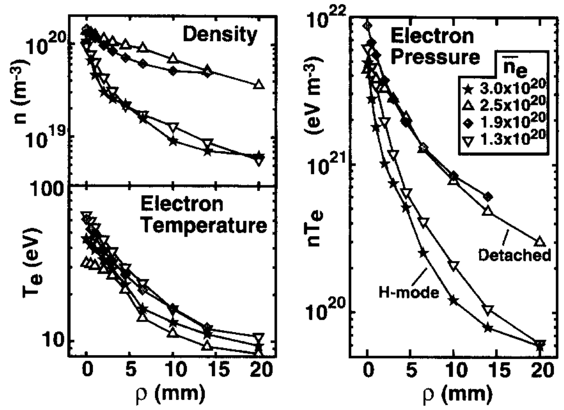

Fig. 5. Cross-field density, electron temperature and electron pressure profiles at the fast-scanning probe location. The cross-field coordinate, ρ, labels the local flux surface according to its distance outside the LCFS at the plasma midplane.

4. Model for parallel and cross-field heat transport

The goal of divertor/SOL transport studies is to formulate physics-based transport relationships that are capable of reproducing experimental observations, such as those illustrated in Fig. 5. This task requires consideration of both cross-field and parallel transport mechanisms. Cross-field transport is anomalous, with the underlying transport mechanisms remaining to be identified. Consequently, a direct, experimental parameterization of the magnitude of cross-field transport in terms of local values of density, temperature, magnetic field, etc. would be most desirable. On the other hand, parallel transport appears to be appropriately described by classical processes: classical electron conduction yields estimates of parallel currents and heat fluxes that are consistent with experiment. Assuming parallel transport is classical, it is possible to determine the level of anomalous perpendicular transport by examining the cross-field density and temperature profiles. This approach, in its simplest form, is used in Section 5 to determine the scaling of local cross-field heat transport with local plasma conditions.

The transport model considered here [27] is similar to an 'onion skin' model [28,29], where parallel transport is modeled as a 1D fluid system with effective sources and sinks from cross-field transport. Typically, volumetric losses (radiation) are separately specified. However, in the model considered here, volumetric losses are estimated directly from the simultaneous measurements of plasma conditions upstream and at the divertor surface.

4.1. Parallel heat transport and divertor radiation

Conservation of energy requires

$$\nabla_{\|} q_{\|} + \nabla_{\perp} q_{\perp} + Q_{\mathrm{Rad}} = 0, \tag{1}$$

where $q_{\|}$ in the bulk plasma is assumed to be dominated by electron parallel conduction, $q_{\|} \cong (2/7)\kappa_0 \nabla_{\|} T^{7/2}$. This approximation is valid over most of the SOL since significant parallel convection is principally restricted to the recycling zone near the divertor plates. $q_{\|}$ at the sheath is given by

$$q_{\|}\big|_{\mathrm{sheath}} = e\gamma n_{\mathrm{d}} T_{\mathrm{d}}^{3/2} \sqrt{\frac{2e}{m_{\mathrm{i}}}}\,. \tag{2}$$

Here, κ_0 is 2.8×10^3 W m^{-1} eV$^{-7/2}$, e is 1.6×10^{-19} J eV^{-1}, and γ is the sheath heat transfer coefficient. Subscripts 'd' refer to conditions at the divertor plate.

The edge plasma can be decomposed into a series of adjacent flux tubes, each with length L, extending from the symmetry point, $S = 0$, to the divertor surface, $S = L$. Integrating Eq. (1) over the flux tube,

$$\begin{aligned} q_{\|}\big|_{\mathrm{sheath}} &= -\langle \nabla_{\perp} q_{\perp} \rangle L' - \int_0^L Q_{\mathrm{Rad}}\, \mathrm{d}S \\ &= -(1 - f_{\mathrm{Rad}}) \langle \nabla_{\perp} q_{\perp} \rangle L', \end{aligned} \tag{3}$$

where f_{Rad} is defined as the fraction of total power into the flux tube that is lost from volumetric processes (radiation) rather than conducted to the sheath. $\langle \nabla_{\perp} q_{\perp} \rangle$ represents an average value along the flux tube's length over a distance L'. L' is defined as the length of the flux tube outside the divertor region. In this formulation, $\nabla_{\perp} q_{\perp}$ is approximated as zero in the region of $S > L'$ where the flux tubes become adjacent to the private flux zone.

The temperature upstream from the divertor can be obtained from integrating Eq. (1) twice and by assuming a profile for the volumetric losses. Modeling the volumetric losses as a decreasing function of distance from the divertor plate,

$$Q_{\mathrm{Rad}} = Q_0 \mathrm{e}^{(S-L)/\lambda_{\mathrm{R}}}, \tag{4}$$

the upstream temperature is

$$\begin{aligned} T^{7/2} &= T_{\mathrm{d}}^{7/2} - \frac{7}{4\kappa_0} \langle \nabla_{\perp} q_{\perp} \rangle L'^2 \\ &\quad \times \left\{ \frac{2L}{L'} - 1 - \frac{S^2}{L'^2} - \frac{f_{\mathrm{Rad}} 2\lambda_{\mathrm{R}}}{(1 - \mathrm{e}^{-L/\lambda_{\mathrm{R}}}) L'} \right. \\ &\quad \left. \times \left[1 + \frac{S-L}{\lambda_{\mathrm{R}}} \mathrm{e}^{-L/\lambda_{\mathrm{R}}} - \mathrm{e}^{(S-L)/\lambda_{\mathrm{R}}} \right] \right\}. \end{aligned} \tag{5}$$

This expression is valid for $S < L'$. Typical values of L, L', and S at the scanning probe location for the discharges studied here are 12, 10, and 7 meters, respectively. The curly bracketed term in Eq. (5) is a weak function of f_{Rad} and λ_{R} for values of S that correspond to the scanning probe location. For attached divertor discharges with $\lambda_{\mathrm{R}} \cong 2$ meters and $0 < f_{\mathrm{Rad}} < 0.5$, this term has a value of ~ 0.8.

4.2. Cross-field heat transport

Although the magnitude of cross-field transport is presently not calculable from first principles, cross-field fluxes are often modeled to be diffusive, proportional to the local density and temperature gradients. Assuming that $\chi_{\perp}^{\mathrm{i}} \cong \chi_{\perp}^{\mathrm{e}}$, the cross field heat flux can be written as the sum of conduction and convection terms,

$$\begin{aligned} q_{\perp} &= q_{\perp}^{\mathrm{i}} + q_{\perp}^{\mathrm{e}} \\ &= -\chi_{\perp} n \nabla_{\perp} (T_{\mathrm{i}} + T_{\mathrm{e}}) - \tfrac{5}{2} (T_{\mathrm{i}} + T_{\mathrm{e}}) D_{\perp} \nabla_{\perp} n. \end{aligned} \tag{6}$$

Setting $D_{\perp}$ to be locally proportional to $\chi_{\perp}$, $D_{\perp} \cong \beta(2/5)\chi_{\perp}$, and $T_{\mathrm{i}} \approx T_{\mathrm{e}}$,

$$\nabla_{\perp} q_{\perp} \cong -2 \nabla_{\perp} \chi_{\perp} [\nabla_{\perp} n T_{\mathrm{e}} + (\beta - 1) T_{\mathrm{e}} \nabla_{\perp} n]. \tag{7}$$

For the case when $\beta \approx 1$, the cross-field heat flux in the SOL is proportional to the local pressure gradient. Results from 2D fluid modeling of SOL plasmas in Alcator C-Mod [21,30] produce $D_{\perp} \approx 0.2$–$0.8 \chi_{\perp}$, implying that $\beta \approx 1$ is not a bad first approximation.

An effective local cross-field transport gradient scale length, λ_{tr}, can be defined as

$$\frac{1}{\lambda_{\mathrm{tr}}} = \frac{1}{\lambda_T} + \frac{\beta}{\lambda_n} \tag{8}$$

such that

$$q_{\perp} = -2 \chi_{\perp} n T_{\mathrm{e}} / \lambda_{\mathrm{tr}}. \tag{9}$$

4.3. Expected scaling of λ_p with T_e

In the high-recycling regime, Eqs. (5) and (7) with $\beta \approx 1$ imply that the local transport gradient scale length ($\sim \lambda_p$) at the scanning probe location should scale with the upstream electron temperature, the electron pressure on the flux surface, and the average value of $\chi_{\perp}$ on the flux surface. The possible complication of $\chi_{\perp}$ varying across flux surfaces can be crudely considered by postulating $\chi_{\perp} \cong \chi_{0\perp} [(nT_{\mathrm{e}})/(n_0 T_{\mathrm{e}0})]^{\alpha}$. Approximating $\nabla_{\perp}^2 n T_{\mathrm{e}} \cong n T_{\mathrm{e}} / \lambda_p^2$, the transport model yields

$$\lambda_p \approx L' \left(\frac{7eg(\alpha + 1)\chi_{0\perp}}{2\kappa_0 n_0^{\alpha} T_{\mathrm{e}0}^{\alpha}} \right)^{1/2} n^{(\alpha+1)/2} T_{\mathrm{e}}^{(2\alpha-5)/4} \tag{10}$$

with the restriction that $\alpha > -1$. Here, the values n and T_{e} refer to conditions 'upstream' near the scanning probe location. Averaging over the flux tube length, one obtains the geometrical factor, g (~ 0.25), which accounts for distortion in the flux tube's cross-section as it wraps around the core plasma. For values of α less than ~ 1, we expect to see a strong inverse relationship between the local pressure enfolding length and the local electron temperature. The data does indeed show this behavior.

5. Measurements and empirical scalings of λ_n, λ_T, and λ_p

5.1. General observations in L-mode discharges

5.1.1. Open divertor bypass

Fig. 6 plots local density, electron temperature, and electron pressure gradient scale lengths (mapped to the midplane) as a function of the local electron temperature at the scanning probe location. These data were taken from 45 ohmic, L-mode discharges (0.8 MA, 5.3 T, $0.7 \leq \bar{n}_e \leq 2.1 \times 10^{20}$ m^{-3}). The divertor bypass leak was open and no boronization was employed. Measurements taken on 7 different flux surface locations for each discharge are shown: ρ = 1, 2, 3, 4.5, 6.5, and 10 mm. The local parallel transport regime is labeled (where possible) according to the measurements of upstream and outer divertor conditions:

$\cdot T_e^{div}/T_e^{up} < 0.5$	high-recycling,
$\cdot T_e^{div}/T_e^{up} > 0.8$	low-recycling,
$\cdot 2nT_e^{div}/nT_e^{up} < 0.4$	detached,
$\cdot 2nT_e^{div}/nT_e^{up} > 1.7$	death-ray.

Data points lacking the corresponding divertor measurements (shown as diamonds in Figs. 6 and 7) are not labeled.

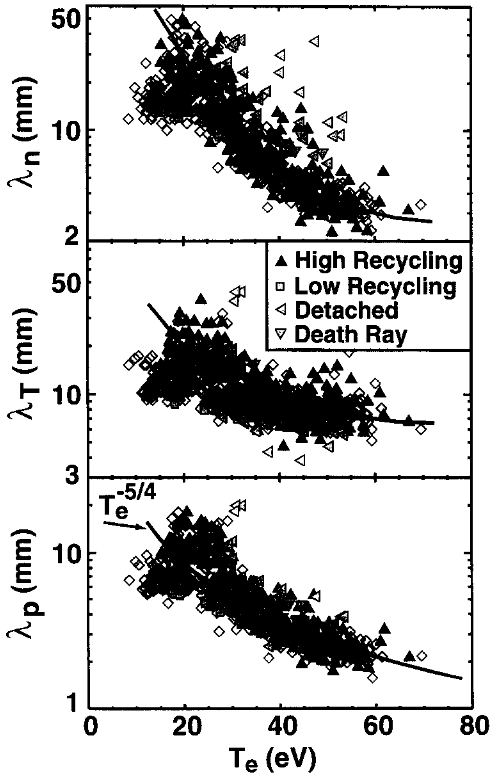

Fig. 6. Local density (λ_n), electron temperature (λ_T), and electron pressure cross-field gradient scale length (λ_p) versus local electron temperature (T_e) at the scanning probe location. These data were taken with the divertor bypass open and no boronization.

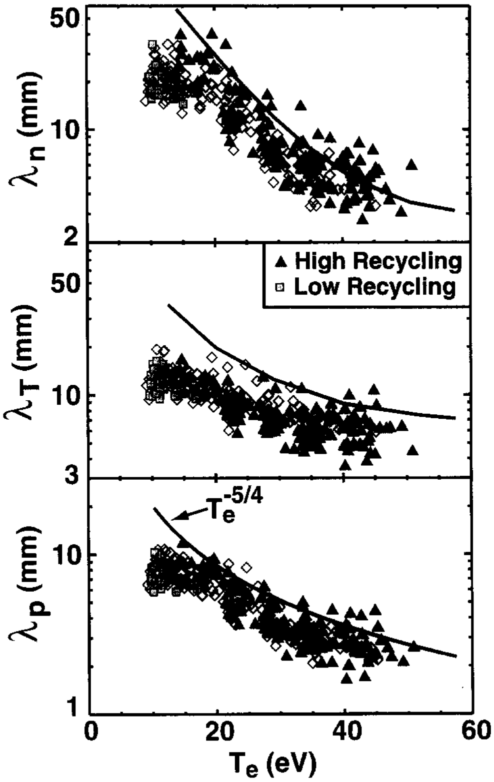

Fig. 7. Similar to Fig. 6 for discharges with the divertor bypass closed. The solid lines are the same as those shown in Fig. 6.

All three gradient scale lengths generally show an inverse dependence on the local electron temperature. The pressure gradient scale length exhibits less scatter than the other two, perhaps indicating that this parameter is more representative of the effective cross-field transport scale length.

A curve proportional to $T_e^{-5/4}$ is shown on the λ_p plot for reference. These results reinforce the idea that cross-field heat transport is proportional to a local transport gradient (~ $1/\lambda_p$) and is balanced primarily by classical parallel electron heat conduction, i.e., Eq. (10).

Solid lines are drawn through the high-recycling data points on the λ_T and λ_n plots, showing the overall trend and allowing a comparison to be made with data in Figs. 7 and 9. Low-recycling data points generally exhibit shorter gradient scale lengths while detached data have longer gradient scale lengths at the same electron temperature. All low-recycling data points on this plot maintain $\lambda_{ei}/L < 0.03$ at the scanning probe location, allowing the parallel heat transport to be described by classical conduction.

5.1.2. Closed divertor bypass

Data from a set of 24 discharges similar to those shown in Fig. 6 were taken after the divertor bypass leak was closed (L-mode, 0.8 MA, 5.3 T, $1.1 \leq \bar{n}_e \leq 2.4 \times 10^{20}$ m^{-3}). Fig. 7 plots these data in the same format as Fig. 6 for comparison (detached data points are not shown). The solid lines of Fig. 6 are in Fig. 7 for comparison. A surprising result is that both the density and temperature gradient scale lengths are significantly reduced in these discharges relative to those in Fig. 6 at the same electron temperatures. This dramatic difference caused us to look into any possible systematic errors in the scanning probe measurements that may have been introduced between the two run campaigns. A possible positioning error of the scanning probe relative to the LCFS is estimated as $\Delta \rho \approx 2$ mm (corresponding to a variation in T_e at the 'separatrix' of 30%). However, such a systematic error could not account for the change in the observed relationships between the local gradient scale lengths and the local electron temperature. Other possible effects such as changes in the voltage bias waveforms and changes in noise fluctuation levels were also investigated. The only systematic difference was the changeover from molybdenum probe electrodes (open divertor bypass) to tungsten electrodes (closed divertor bypass). However, this change should not significantly effect the I–V characteristic and especially not affect the inferred local density and temperature gradient scale lengths.

Accepting these data points as correct, we must conclude that the closing of the divertor bypass leak resulted in increased cross-field temperature and density gradients in the SOL, implying a reduced level of anomalous cross-field transport. This result resembles core confinement observations: H-mode regimes are often more readily accessed when the midplane neutral pressure is lowered, either by closing the divertor [31], controlling gas delivery [32], and/or conditioning the walls to provide low recycling [33]. As a result of closing the divertor bypass leak, the divertor neutral pressure in otherwise similar discharges was increased by a factor of ~ 2.5 while the midplane neutral pressure was reduced by ~ 20%. A more quantitative relationship between cross-field transport and neutral density/ionization sources in the SOL is the subject of ongoing investigation.

5.2. Regression analysis of λ_p

A linear regression analysis procedure was employed to investigate the scaling of cross-field gradients with local plasma conditions for a large set of discharges. Ohmic, L-Mode discharges were sorted into the following three groups:

(a) Open divertor bypass: (75 discharges, 153 data samples) $0.5 \leq \bar{n}_e \leq 2.6 \times 10^{20}$ m^{-3}, $I_p = (0.4, 0.6, 0.8, 1.0$ MA), $B_T = (3.7, 5.3, 7$ T).

(b) Closed divertor bypass: (24 discharges, 60 data samples) $0.7 \leq \bar{n}_e \leq 2.4 \times 10^{20}$ m^{-3}, $I_p = 0.8$ MA, $B_T = 5.3$ T.

(c) Closed divertor bypass, boronized: (130 discharges, 143 data samples) $0.6 \leq \bar{n}_e \leq 2.8 \times 10^{20}$ m^{-3}, $I_p = (0.47, 0.55, 0.8, 1.0, 1.1$ MA), $B_T = (2.8, 4.5, 5.3, 7.0, 7.8$ T).

As suggested by Figs. 6 and 7, the pressure gradient scale length (λ_p) appears to be a reasonable representation of the overall transport gradient scale length. A power law formula for the perturbation of λ_p about a mean value, λ_p^* was assumed,

$$\lambda_p = \lambda_p^* (T_e/50)^{\alpha} (n/10^{20})^{\beta} (L/12.5)^{\gamma} (B_T/5)^{\delta}, \quad (11)$$

where: T_e-electron temperature at the scanning probe location (eV), n-plasma density at the scanning probe location (m^{-3}), $L - 1/2$ of total connection length (m), B_T-toroidal magnetic field on axis (T). No allowance is made for a possible explicit dependence of λ_p on flux surface position since a strong covariance of ρ with local n and T_e exists in the data. A strong covariance also exists between the plasma current and the connection length. Any explicit dependence of λ_p on poloidal magnetic field strength is therefore not resolvable with the present data set.

Fig. 8 shows an example fit to the regression formula for the group (c) data set. Data is included from 6 flux surface locations: $\rho = 1$, 2, 3, 4.5, 6.5, and 10 mm. Only data points in the high-recycling regime (as defined in Section 5.1) were included in this regression. The power law formula does a reasonable job of fitting data points taken over a wide range of discharge conditions.

A surprising result, verified by a detailed statistical analysis discussed below, is that the gradient scale lengths are virtually independent of toroidal magnetic field

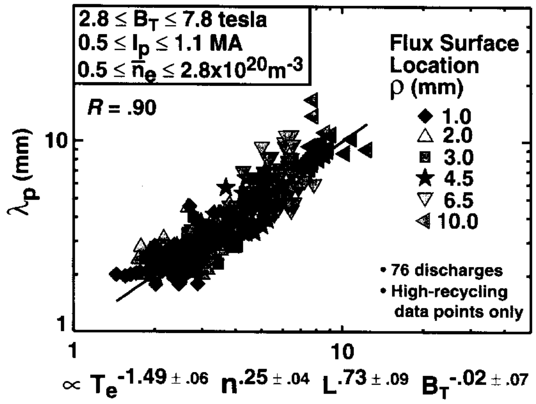

Fig. 8. Regression analysis of local λ_p data from boronized discharges with the divertor bypass closed.

Table 1
Regression analysis: high-recycling data points with $1 \leq \rho \leq 10$ mm

	(a) Open bypass			(b) Closed		(c) Closed, boronized				
λ_p^* (mm)	2.67 ± 0.05	2.87 ± 0.08	3.03 ± 0.08	2.04 ± 0.07	2.22 ± 0.10	2.36 ± 0.04	2.37 ± 0.04	2.48 ± 0.04	2.34 ± 0.04	2.48 ± 0.04
α	-1.36 ± 0.04	-1.43 ± 0.05	-1.66 ± 0.06	-1.21 ± 0.06	-1.28 ± 0.06	-1.04 ± 0.03	-1.13 ± 0.04	-1.49 ± 0.06	-1.15 ± 0.04	-1.49 ± 0.06
β	–	0.13 ± 0.04	0.18 ± 0.09	–	0.21 ± 0.07	–	0.14 ± 0.04	0.25 ± 0.04	0.15 ± 0.04	0.25 ± 0.04
γ	–	–	0.55 ± 0.09	–	–	–	–	0.72 ± 0.09	–	0.73 ± 0.09
δ	–	–	–	–	–	–	–	–	0.13 ± 0.07	-0.02 ± 0.07
R	0.866	0.872	0.885	0.871	0.880	0.877	0.880	0.899	0.881	0.899
χ_R^2	1.95	1.89	1.90	0.799	0.720	1.43	1.38	1.14	1.38	1.14

$\lambda_p = \lambda_p^*(T_e/50\text{ eV})^{\alpha}(n/10^{20}\text{ m}^{-3})^{\beta}(L/12.5\text{ m})^{\gamma}(B_T/5\text{ T})^{\delta}$.

Table 2
Regression analysis: all data points spanning $1 \leq \rho \leq 4.5$ mm

	(a) Open bypass					(b) Closed		(c) Closed, boronized				
λ_p^* (mm)	2.73 ± 0.05	3.17 ± 0.07	3.19 ± 0.07	2.98 ± 0.07	3.12 ± 0.07	1.98 ± 0.08	2.33 ± 0.10	2.35 ± 0.04	2.43 ± 0.04	2.50 ± 0.04	2.36 ± 0.04	2.43 ± 0.04
α	-1.45 ± 0.05	-1.42 ± 0.05	-1.68 ± 0.05	-1.47 ± 0.05	-1.67 ± 0.05	-1.37 ± 0.07	-1.35 ± 0.06	-0.85 ± 0.04	-1.07 ± 0.05	-1.38 ± 0.06	-1.19 ± 0.05	-1.40 ± 0.06
β	–	0.16 ± 0.02	0.19 ± 0.02	0.17 ± 0.02	0.19 ± 0.02	–	$0.26 \pm .04$	–	0.18 ± 0.02	0.25 ± 0.02	0.17 ± 0.02	0.23 ± 0.02
γ	–	–	0.67 ± 0.06	–	0.59 ± 0.07	–	–	–	–	0.61 ± 0.07	–	0.50 ± 0.07
δ	–	–	–	0.76 ± 0.10	0.26 ± 0.11	–	–	–	–	–	0.29 ± 0.04	0.21 ± 0.04
R	0.747	0.780	0.826	0.803	0.828	0.809	0.847	0.620	0.670	0.718	0.706	0.734
χ_R^2	3.32	2.99	2.50	2.76	2.50	2.73	2.32	2.01	1.83	1.56	1.75	1.55

$\lambda_p = \lambda_p^*(T_e/50\text{ eV})^{\alpha}(n/10^{20}\text{ m}^{-3})^{\beta}(L/12.5\text{ m})^{\gamma}(B_T/5\text{ T})^{\delta}$.

strength. This is despite the large range in toroidal field ($2.8 \leq B_T \leq 7.8$ T) included in the data set. One might anticipate that the gradient scale lengths would exhibit an inverse dependence on B_T (e.g., Bohm or classical transport). However, these data suggest no dependence on B_T.

Tables 1 and 2 summarize the results from regression analysis of all three discharge groups. Table 1 only includes points in the high-recycling regime for flux surface locations $\rho = 1$, 2, 3, 4.5, 6.5, and 10 mm. Table 2 includes all data points from flux surface locations $\rho = 1$, 2, 3, and 4.5 mm. The rows labeled R and χ_R^2 are respectively the multiple correlation coefficients and the sample variances of the fits [34]. Tables 1 and 2 track these statistical parameters as successive terms are added to the regression. One can see from section (c) of Table 1 and sections (a) and (c) of Table 2 that the dependence of λ_p on B_T and L can be separately resolved by the statistics of these data sets. R is maximized and χ_R^2 is minimized when both B_T and L terms are included (leading to small values of δ), or when the B_T term is excluded (implying $\delta = 0$). Similar coefficients are obtained in Tables 1 and 2, indicating that the flux surface location of the data sample has little influence on the results.

The regression analysis of λ_p confirms trends that can be seen in the raw data: (1) a strong inverse dependence on T_e, similar to that expected from classical parallel electron conduction, (2) a weak dependence on density, (3) a weaker than expected dependence on L, and (4) little or no dependence on B_T. Combining the results from the tables, the power law formulas for λ_p are roughly:

Open divertor bypass:

$$\lambda_p\,(\mathrm{mm}) \cong 3.1(T_e/50)^{-1.7}(n/10^{20})^{0.2}(L/12.5)^{0.6}. \tag{12}$$

Closed divertor bypass:

$$\lambda_p\,(\mathrm{mm}) \approx 2.5(T_e/50)^{-1.4}(n/10^{20})^{0.25}(L/12.5)^{0.65}. \tag{13}$$

From Eq. (10), these results suggests that $\chi_\perp$ scales approximately as

$$\chi_\perp \propto T_e^{-0.6} n^{-0.6} L^{-0.7}. \tag{14}$$

The inverse dependence on connection length derives from the weak dependence of λ_p on L.

5.3. Observations of gradient scale lengths in H-mode discharges

The gradient scale lengths in H-mode discharges dramatically depart from the empirical scaling 'rules' developed above. Fig. 9 plots cross-field gradient scale lengths in a similar format to Figs. 6 and 7 for a series of RF-heated H-mode discharges ($B_T = 5.3$ T, $0.8 \leq I_p \leq 1.1$ MA, $2.0 \leq \bar{n}_e \leq 3.6 \times 10^{20}$ m^{-3}). The solid lines of Fig. 6 are shown in Fig. 9 for comparison. All discharges had the divertor bypass leak closed and boronized walls. The flux surface locations of the measurements are indicated by the symbols. Pressure gradient scale lengths near the separatrix are reduced by a factor of ~ 2 relative to L-mode, down to a level of 1 mm and remain at that level despite a large variation (factor of ~ 2) in the local T_e. These remarkably small scale lengths are only a few times an ion gyro radius ($\rho_i \sim 0.25$ mm for 100 eV ion) and comparable to an ion banana width ($\Delta b \sim 1.4$ mm). Further out into the SOL ($\rho > 4.5$ mm), the data points generally follow the L-mode scaling 'rule' (divertor bypass closed, e.g., Fig. 7).

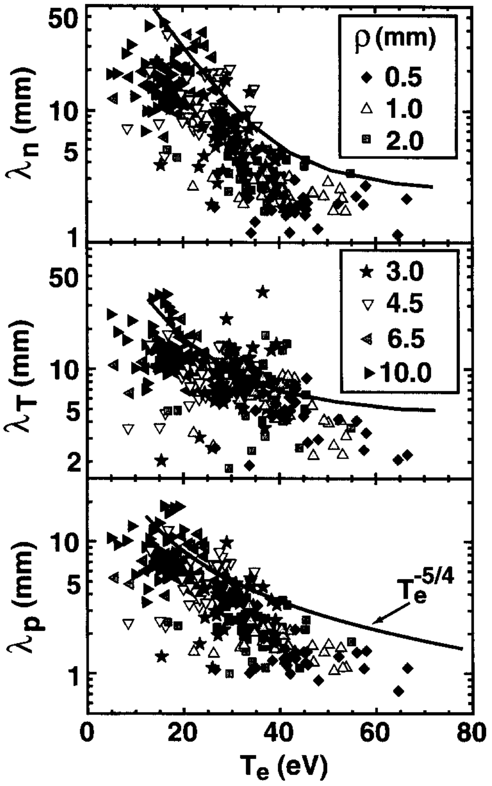

Fig. 9. Similar to Fig. 6 for boronized, H-mode discharges with the divertor bypass closed. Different symbols indicate the flux surface location of each measurement. The solid lines are the same as those show in Fig. 6.

Unlike in ohmic, L-mode plasmas, the gradient scale lengths near the separatrix appear to depend more on flux surface location than on the magnitude of the parallel heat transport. Apparently, the H-mode transport barrier, which is known to exist in the vicinity of the separatrix, also extends partly into the SOL region. An understanding of cross-field transport in the SOL may therefore also require an understanding of H-mode transport barrier physics. More detailed analyses of H-mode SOL transport phenomena in Alcator C-Mod await further experimentation.

6. Estimates of cross-field $\chi_\perp$ profiles

Measurements of the temperature and density profiles can be used to estimate the cross-field $\chi_\perp$ profile. For a specified value of λ_R, Eqs. (2), (3) and (5), yield an estimate of the f_{Rad} profile. (An example is shown in Fig. 3(e).) The $q_\perp(\rho)$ profile can then be obtained from Eq. (5) by integrating $\langle\nabla_\perp q_\perp\rangle$ from ρ to ∞. $\chi_\perp(\rho)$ is then deduced from Eq. (9),

$$\chi_\perp(\rho) = \frac{-\lambda_{tr}(\rho)}{2gn(\rho)T_e\rho)}\bigg|_{mid}\int_\rho^\infty \langle\nabla_\perp q_\perp\rangle \mathrm{d}\rho', \qquad (15)$$

where the geometrical factor, g (~ 0.25) results from averaging $\langle\dots\rangle$ the cross-field heat flux over the length of the flux tube. The average is exact when $\lambda_{tr} = \lambda_p$ (i.e., $\beta = 1$), since it assumes that pressure is constant on flux surfaces outside the divertor region. However, for $\beta \neq 1$, Eq. (17) still applies when density and temperature are approximately constant on these flux surfaces. Since Eq. (15) primarily involves measurements of λ_{tr}, n, and T_e made by the scanning probe, the inferred $\chi_\perp$ profile is insensitive to any errors in the relative positioning of the scanning probe and the LCFS.

The integrand in Eq. (15) is defined only on flux surfaces in which measurements were taken. Therefore, an assumption must be made about $q_\perp$ at the measurement boundary, $q_\perp(\rho = \rho_{max})$. Since $q_\perp$ decays exponentially with ρ, estimates of $\chi_\perp$ near the separatrix are insensitive to any reasonable estimate of $q_\perp(\rho_{max})$. However, $\chi_\perp$ becomes increasingly sensitive to $q_\perp(\rho_{max})$ as ρ approaches ρ_{max}. For the data shown below, $q_\perp(\rho_{max})$ was chosen to minimize the curvature in the inferred $\chi_\perp(\rho)$ profile, weighted by the relative error bar on $\chi_\perp(\rho)$. Values of $\chi_\perp$ near the measurement boundary ($\rho \gtrsim 14$ mm) are not reported since they are entirely determined by this choice of $q_\perp(\rho_{max})$.

The cross-hatched regions in Fig. 10 show the overall range in $\chi_\perp$ computed for three sets of discharges: L-mode with open divertor bypass, L-mode with closed divertor bypass, and H-mode with closed divertor bypass. The 93 discharges had $B_T = 5.3$ T, $0.8 \leq I_p \leq 1.1$ MA, and spanned a range of densities, $0.6 \leq \bar{n}_e \leq 3.2 \times 10^{20}$ m^{-3}. For the L-mode plasmas, both attached and detached divertor discharges are included. The H-mode data do not include detached divertor discharges. The assumption of $\beta \approx 1(\lambda_{tr} \approx \lambda_p)$ was employed for these estimates.

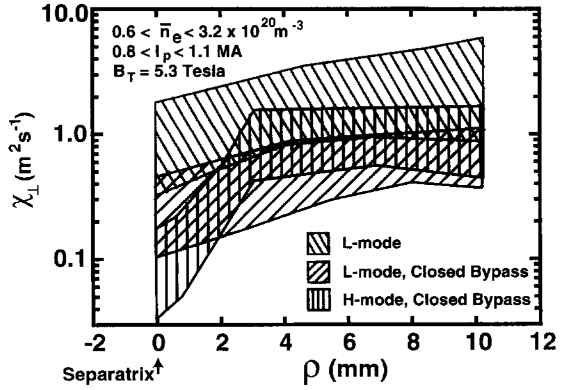

Fig. 10. Cross-field profiles of $\chi_\perp$ inferred from transport model with $\beta = 1$.

The factor of ~ 3 vertical extent of the cross-hatched regions is a consequence of the high level of scatter in the experimental input parameters such as $T_e^{7/2}$ and $\nabla_\perp nT_e$. Nevertheless, some clear trends are evident.

(1) $\chi_\perp$ generally increases with increasing ρ. On average, the L-mode plasmas show a factor of ~ 3 increase over the 10 mm SOL width.

(2) The H-mode plasmas have a dramatic factor of ~ 10 increase over the first 3 mm of the SOL, then remain relatively flat outside this region.

(3) $\chi_\perp$ at the separatrix depends on confinement mode and, apparently, the neutral particle retention characteristics of the divector: $\chi_\perp$ at the saparatrix is reduced from ~ 0.8 to ~ 0.25 m^2 s^{-1} by simply closing the divertor bypass leak. H-mode discharges show an additional drop in $\chi_\perp$ at the separatrix, down to values of ~ 0.08 m^2 s^{-1}

The variation in $\chi_\perp$ across the profile for L-mode discharges is consistent with the results from the regression analysis. Although Eq. (14) does not have an explicit dependence on flux surface location, the correlation $\chi_\perp \sim (nT_e)^{-0.6}$ yields a factor of ~ 2.5 to ~ 7 increase in $\chi_\perp$ over a 10 mm SOL width for typical pressure profiles (e.g., Fig. 5).

6.1. Sensitivity of $\chi_\perp$ estimate to transport assumptions

The values for $\chi_\perp$ reported in Fig. 10 rely on a number of assumptions: (1) $\beta \approx 1$, (2) β is independent of ρ, and (3) cross-field heat transport is primarily diffusive, proportional to cross-field density and temperature gradients.

(1) Recomputing the $\chi_\perp$ profiles in Fig. 10 with $\beta = 0.1$ and 10.0 (corresponding to $D_\perp/\chi_\perp = 0.04$ and 4.0), the absolute level of $\chi_\perp$ is affected by a corresponding factor of ~ 3 and ~ 0.1. However, the overall shape of the profiles remains unchanged. Most importantly, the relative magnitudes of $\chi_\perp$ for the three discharge groups shown in Fig. 10 remain unchanged.

(2) In principle, the ratio of $D_\perp/\chi_\perp$ could vary across the SOL. For example, H-mode discharges might have a constant $\chi_\perp$ profile yet have a $D_\perp$ profile that varies strongly with ρ. This possibility can not be excluded at present.

(3) The observation that local values of λ_n and λ_T scale with local electron temperature in L-mode discharges suggests that cross-field heat transport is primarily composed of diffusive components (see Section 5). However, one can not exclude the possibility of non-local transport

contributions such as a velocity pinch. This is particularly a concern near the separatrix in H-mode discharges, where a simple relationship between local gradient scale lengths and local electron temperature is not observed.

7. Asymmetric parallel transport

In any tokamak SOL plasma, it is natural to expect some level of asymmetry in the cross-field transport of heat and particles. Effects such as toroidal geometry, magnetic flux surface compression, classical cross-field drifts, and poloidally asymmetric anomalous transport can contribute. Asymmetric heat fluxes to the inner and outer divertor legs, observed in a number of experiments [35–38], have often been ascribed to these kinds of effects. In contrast, asymmetric *parallel* transport has received relatively little attention. Yet, one can not assume that parallel heat and particle transport is inherently symmetric. For example, currents flowing along field lines can contribute to asymmetric parallel heat fluxes. In the case of particle flows, imbalanced ionization sources can drive asymmetric parallel particle fluxes.

Experimental observations presented in this section suggest that asymmetric parallel heat transport may indeed play an important role in initiating and/or maintaining the inside/outside divertor asymmetries in Alcator C-Mod. Once the heat flux asymmetry is established, an accompanying asymmetry in the local ionization source may also explain an observed parallel flow asymmetry: divertor flow reversal.

7.1. Inside / outside divertor asymmetries

Detailed measurements of the inside/outside divertor asymmetry in Alcator C-Mod have been made with Langmuir probe systems, TV survey cameras, and tomographic bolometer and H_α systems. Some of these observations have been reported previously [6]. Continuing experimentation and analysis is in progress.

Fig. 11 shows cross-field profiles of electron stagnation pressure, electron temperature, and density at three poloidal locations: scanning probe ('upstream'), outer divertor surface and inner divertor surface. Data are shown from two ohmic, L-mode discharges (5.3 T, 0.8 MA, $\bar{n}_e = 0.9 \times 10^{20}$ m^{-3}). With B_T in the normal direction ($B \times \nabla B$ ion drift towards the x-point), the outer divertor is significantly hotter than the inner divertor (factor of 5–10). On the other hand, the density is lower on the outer divertor such that the electron stagnation pressure is approximately the same and matches the pressure at the scanning probe location. With reversed B_T, the inner divertor generally becomes hotter than the outer divertor. The density asymmetry also reverses so that again the electron stagnation pressure approximately matches.

Fig. 12 shows the dependence of the asymmetry on edge plasma conditions, as recorded by the outside/inside temperature and density ratios (Fig. 12(a), (b)) on the $\rho = 4.5$ mm flux surface. Ohmic, L-mode discharges are shown (5.3 T, 0.8 MA, $0.6 \leq \bar{n}_e \leq 2.1 \times 10^{20}$ m^{-3}). The horizontal axis is the electron–ion mean free path at the scanning probe location ($\rho = 4.5$ mm), normalized to 1/2 the total parallel connection length (λ_{ei}/L). Low density discharges with a hot SOL (high λ_{ei}/L) display a large asymmetry, having outside/inside T_e ratios approaching ~ 10 with normal B_T and ~ 0.2 with reversed B_T. As the collisionality in the SOL increases, the magnitude of the asymmetry decreases, vanishing in the highest density (lowest edge temperature) discharges.

Also shown in Fig. 12 is the ratio of 'grounded' to ion saturation current densities (J_{gnd}/J_{sat}) collected by the outer and inner divertor surfaces at this flux surface location (Fig. 12(c), (d)). J_{gnd} is defined as the current density on a divertor probe when the probe is biased at the potential of the divertor. A positive number indicates a net ion collection locally on the divertor surface. Contributions to J_{gnd} include: parallel currents flowing as a result of the inside/outside electron temperature differences (thermoelectric effect), loop-voltage induced parallel currents, and non-ambipolar currents (such as Pfirsch–Schluter currents) that flow partly parallel to B but complete the electrical circuit via cross-field transport.

Fig. 12(c), (d), show that a significant component of J_{gnd} exhibits a thermoelectric-like effect, scaling with the magnitude of the outside/inside electron temperature asymmetry and reversing when the asymmetry reverses. When the temperature asymmetry is high, J_{gnd} on the hotter divertor surface is negative (net electron collection) with a magnitude that can exceed two times the local ion

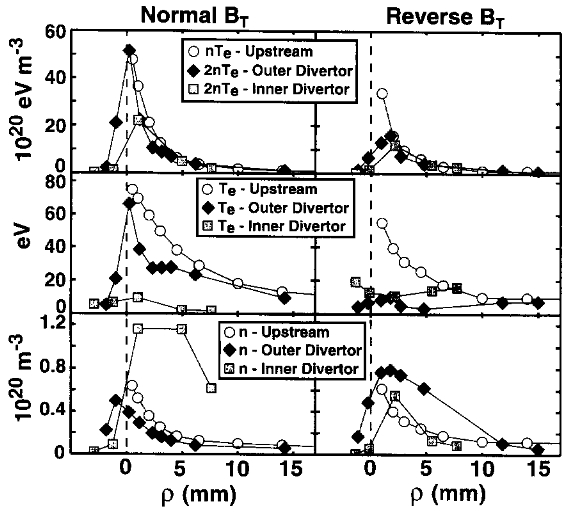

Fig. 11. Electron stagnation pressure, electron temperature and density profiles at scanning probe location and on inner and outer divertor surfaces for forward and reversed B_T directions.

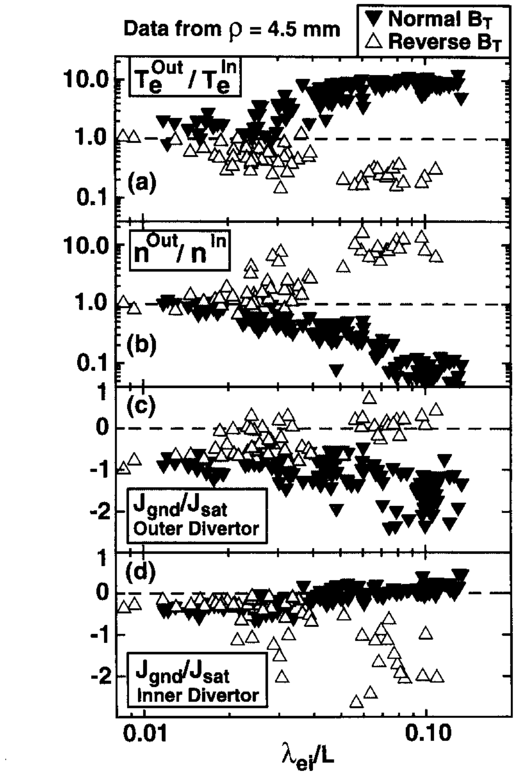

Fig. 12. Divertor measurements on the $\rho = 4.5$ mm flux surface: Outside/inside electron temperature ratio, density ratio, and 'grounded' current density normalized to the ion saturation current density is plotted versus λ_{ei}/L.

saturation current density. When the temperature asymmetry vanishes ($\lambda_{ei}/L \lesssim 0.02$), J_{gnd} becomes independent of the direction of B_T, revealing a residual non-ambipolar component of $J_{gnd}/J_{sat} \sim -0.8$ for the outer and ~ -0.3 for the inner divertor locations.

7.2. Asymmetric heat fluxes resulting from thermoelectric currents

Thermoelectric currents have been observed in the SOL plasmas of a number of tokamaks [39–41]. The magnitude of the current is found to be generally consistent with classical parallel electron conduction and the effective 'bias' that arises from electron temperature differences at the ends of the field line. For a specified potential difference ($\Delta\Phi$) the parallel current ($J_{\parallel}$) satisfies Ohm's law, integrated along the field line,

$$\frac{J_{\parallel}}{J_{sat}} \cong 60\sqrt{\mu}\,\frac{\Delta\Phi\lambda_{ei}^{FSP}}{T_e^{div}L}\left(\frac{T_e^{div}}{T_e^{FSP}}\right)^3\left(\int_0^1\left(\frac{T_e^{div}}{T_e}\right)^{3/2}\mathrm{d}x\right)^{-1}, \tag{16}$$

assuming conservation of parallel current, constant electron stagnation pressure, and approximating $T_e \sim T_e^{div}$, the same value at both ends of the field line. λ_{ei}^{FSP} is the electron–ion mean free path evaluated at the fast-scanning probe location, L is 1/2 the total connection length, μ is the ion mass (amu), and the integral is performed along the field line. Typical values for the integral in the high recycling regime are 0.1–0.2.

An example case of $\Delta\Phi \sim 3\ T_e^{div}$, $T_e^{div} \sim 10$ eV, $T_e^{FSP} \sim 50$ eV, and $\lambda_{ei}/L \sim 0.1$ results in $|J_{\parallel}/J_{sat}| \sim 1.4$, which is comparable to the observed values in Fig. 12. Note that for $\lambda_{ei}/L \lesssim 0.02$, a relatively insignificant current will flow for any reasonable value of the sheath-induced potential difference. This is also consistent with the observations in Fig. 12.

The sum of ion and electron parallel heat fluxes in a Braginskii plasma fluid [42] in which $T_i \cong T_e$ can be written as

$$q_{\parallel}^{Fluid} = eM(5 + M^2)nT_eC_s - \kappa_{\parallel}\nabla_{\parallel}T_e - \left(\tfrac{5}{2} + 0.71\right)T_eJ_{\parallel}, \tag{17}$$

where M is the parallel mach number and C_s is the local sound speed. Parallel ion heat conduction and viscous terms have been ignored since they contribute little to the total heat flux. The $J_{\parallel}$ term accounts for both electron convection and for the heat flux that arises from a non-maxwellian component of the electron distribution function when $J_{\parallel} \neq 0$. Thus, asymmetric parallel heat fluxes can exist ($J_{\parallel} \neq 0$) even when heat/particle sources and sinks are symmetrically distributed along field lines. Although Eq. (17) is only approximately valid near the divertor surface, the magnitude of $q_{\parallel}^{Fluid}$ outside the sheath region ($M \sim 1$) is roughly

$$\frac{q_{\parallel}^{Fluid}}{T_eJ_{sat}} \sim 6 - \frac{\kappa_{\parallel}\nabla_{\parallel}T_e}{T_eJ_{sat}} - 3.21\frac{J_{\parallel}}{J_{sat}}. \tag{18}$$

Expressions based on kinetic analysis of the heat transport through the sheath are well known [43]. Again assuming $T_i \cong T_e$, the total parallel heat flux through the divertor sheath is

$$\frac{q_{\parallel}^{Sheath}}{T_eJ_{sat}} = 2\left(\frac{2-\delta}{1-\delta}\right) + 2.49 + \mathrm{Ln}\left[\frac{\sqrt{\mu}(1-\delta)}{1-(J_{\parallel}/J_{sat})}\right] - \left(\frac{2}{1-\delta}\right)\frac{J_{\parallel}}{J_{sat}}, \tag{19}$$

where δ is the secondary electron emission coefficient.

A consequence of Eqs. (16), (18) and (19) is that a 'thermoelectric instability' can develop in the SOL (Fig. 13). Asymmetric heat fluxes arising from the $J_{\parallel}$ term in Eq. (18) are not directly offset by the corresponding $J_{\parallel}$ term in Eq. (19) for $\delta < 0.38$. Therefore, once a seed current is formed, the resultant asymmetric heat flux in the bulk plasma can preferentially heat one divertor surface relative to the other. The temperature asymmetry can, in

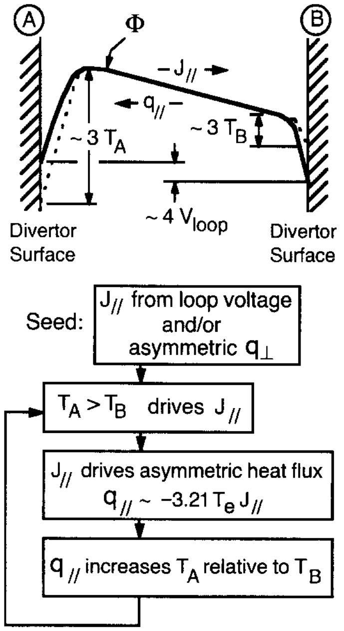

Fig. 13. Thermoelectric heat flux instability mechanism. A parallel 'seed' current (driven by loop voltage) or 'seed' inside/outside temperature asymmetry (driven by cross-field transport asymmetries) can initiate an unstable, positive feedback loop.

turn, cause a larger $J_{\|}$ to flow, leading to a run-away effect. If the electron temperature on the 'hot' divertor surface rises high enough so as to cause $\delta \gtrsim 0.38$, a stable system results. However, the system could stabilize at lower values of T_e on the 'hot' side, as other terms adjust in Eqs. (18) and (19) ($\nabla_{\|} T_e$, for example) to provide the overall fluid-sheath heat flux balance. Divertor radiation can also be an important element in the power balance, modifying the equilibrium state. It is interesting to note that the secondary electron emission coefficient for molybdenum [44] (maxwellian-averaged) exceeds ~ 0.38 at an electron temperature of around 33 eV. Electron temperatures in the 'hot' divertor leg (see Fig. 15) are typically at or below this level.

Fig. 14 evaluates the relative importance of the $J_{\|}$ terms in Eqs. (18) and (19) directly from experimental data with $J_{\|} = J_{\mathrm{gnd}}$. The ratio of $-3.21 T_e J_{\|}/q_{\|}^{\mathrm{Sheath}}$ is plotted in Fig. 14(a), (c), versus λ_{ei}/L. This quantity represents the ratio of fluid heat flux driven by parallel current to total heat flux arriving at the sheath. The ratio $-3.21 T_e J_{\|}/[q_{\|}^{\mathrm{Sheath}} - q_{\|}^{\mathrm{Sheath}}(J_{\|} = 0)]$, which represents the ratio of fluid to sheath heat flux components that depend explicitly on $J_{\|}$ is plotted in Fig. 14(b), (d). The $-3.21 T_e J_{\|}$ term is seen to account for up to half of the total heat flux arriving on the 'hotter' divertor surface. The ratio of fluid to sheath components exceeds a factor of ~ 2 for most of the data points. For data points in which the local divertor is 'hot' ($T_e \gtrsim 20$ eV, $\lambda_{ei}/L \gtrsim 0.1$), this ratio approaches a value closer to ~ 1.

These data indicate that asymmetric heat fluxes in the bulk plasma due to parallel currents significantly contribute to the total heat flux arriving at the divertor surfaces. A large component of the parallel current is driven by thermoelectric effects. The combined phenomena may be responsible for the observed inside/outside temperature and density asymmetries.

Finally, one can speculate on the role of toroidal loop voltage in providing a 'seed current' for the instability. As suggested in Fig. 13, 4–6 V can be expected to appear along magnetic field lines since the current path (including vacuum vessel) encircles the central solenoid about four times in the SOL. This may be sufficient to initiate the inside/outside asymmetry. (One should be cautious, however, since cross-field heat flux asymmetries could dominate over this 'seed' mechanism.) Experimentally, it is observed that the inside/outside asymmetry in single null plasmas produces a hot outer divertor when the $B \times \nabla B$ ion drift is towards the x-point. The asymmetry reverses when B_T is reversed. Owing to the inherent magnetic topology of the tokamak plasma, loop voltage-induced currents in a single null SOL always flow from the outer

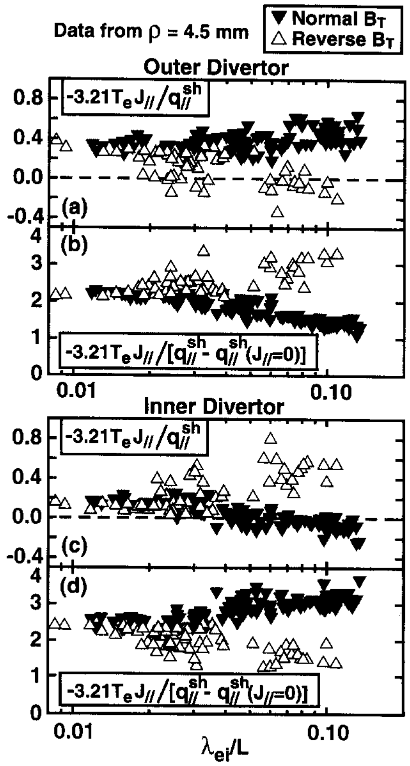

Fig. 14. Evaluation of parallel heat flux transport terms at the outer and inner divertor surfaces on the $\rho = 4.5$ mm flux surface: (a) and (c) $J_{\|}$-driven fluid heat flux ($-3.21 T_e J_{\|}$) normalized to the total parallel heat flux arriving at the divertor sheath, (b) and (d) same fluid heat flux normalized to the component of the sheath heat flux that depends explicitly on $J_{\|}$.

divertor to the inner divertor when the $B \times \nabla B$ ion drift is towards the x-point (independent of both I_p direction and upper/lower x-point position). Such a seed current would cause the outer divertor to be 'hotter', as observed. The inside/outside direction of the seed current (and therefore the asymmetry) reverses only with B_T reversal.

7.3. Reversed parallel plasma flows

The fast-scanning probe can be operated as a Mach probe, recording parallel plasma flow velocity profiles at a location that is 'upstream' from the outer divertor leg (see Fig. 1). The flow direction and approximate Mach number can be inferred from the ratio of upstream/downstream ion saturation currents recorded by two directional probes. Reversed parallel flows (directed away from the divertor surface) near the separatrix are routinely detected for discharges in which the inside/outside asymmetry favors a 'hotter' divertor on the outside.

Fig. 15 shows results from a from a series of ohmic, L-mode, discharges with $B_T = 5.3$ T and $I_p = 0.8$ MA. Electron temperatures at the (a) outer and (b) inner divertor surfaces ($\rho = 3$ mm) and (c) the ratio of ion saturation currents, $J_{sat}^{up}/J_{sat}^{down}$, recorded by the scanning probe near the separatrix ($\rho = 0.5$ mm) are plotted as a function of core line-averaged electron density. As discussed in Section 7.1, the electron temperature at the divertor surfaces depend on both the direction of B_T and the line-averaged density (SOL collisionality). Values of $J_{sat}^{up}/J_{sat}^{down}$ below 1 indicate a reversed flow, i.e., a parallel plasma flow directed *away* from the outer divertor surface. A reversed flow condition is seen for the normal B_T direction whenever the outer divertor is hotter than the inner divertor. For reversed B_T, the outer divertor is never significantly hotter than the inner divertor. Correspondingly, no flow reversal is seen.

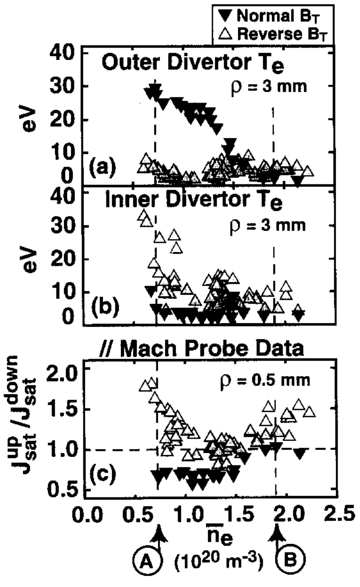

Fig. 15. Electron temperatures at the (a) outer and (b) inner divertor surfaces ($\rho = 3$ mm flux surface) and (c) upstream/downstream ratio of ion saturation currents recorded by the fast-scanning probe on the $\rho = 0.5$ mm flux surface. The horizontal axis is line-averaged density. Parallel mach number profiles taken at densities (A) and (B) are shown in Fig. 16.

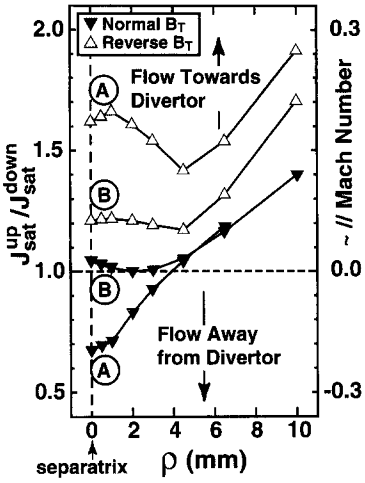

Fig. 16. Cross-field profiles of ion saturation current density ratio recorded by the fast-scanning probe. A ratio less than 1 implies a parallel plasma flow directed away from the outer divertor surface (reverse flow condition). Profiles taken at two densities, (A) 0.7×10^{20} m^{-3}, and (B) 1.9×10^{20} m^{-3}, are shown for forward and reverse B_T directions.

Fig. 16 shows four representative cross-field profiles of $J_{sat}^{up}/J_{sat}^{down}$ at the two densities indicated on Fig. 15: (A) 0.7×10^{20} m^{-3} and (B) 1.9×10^{20} m^{-3}. An estimate of the parallel mach number based on the Hutchinson [45] model is also shown. The observations can be summarized as follows: (1) Reversed B_T – The flow profile is seen to be everywhere directed towards the outer divertor. In this case, the largest parallel flow occurs at low plasma densities when the inner divertor becomes significantly hotter than the outer divertor. (2) Normal B_T – In contrast, these discharges exhibit a generally lower velocity profile, becoming negative (reversed flow) in some regions. Flow reversal occurs near the separatrix ($\rho < 4$ mm) in low density discharges when the outer divertor becomes significantly hotter than the inner divertor. (3) Both directions of B_T – the flow profiles become nearly the same at high plasma densities (case of minimal inside/outside asymmetry).

At first glance, the reversed flow profile shown in Fig. 16 fits the expected picture of flow reversal in a divertor. A local convection loop is formed: preferential ionization near the strike point causes reversed parallel flows to form near the separatrix, cross-field diffusion carries these particles further out into the SOL, and normal parallel flow carries the particles back to the divertor surface. However, the observation that there is no flow reversal in the outer divertor for some discharges (particularly those with reversed B_T) suggests an alternative convection loop: preferential ionization in the hotter divertor leg results in a parallel plasma flow directed towards the colder divertor leg. The resultant convection loop encircles the entire core plasma!

Neutral particles in the private flux zone have potentially equal access to both divertor legs. However, the ratio of charge exchange to ionization rate is a strong function of electron temperature for $T_e \lesssim 30$ eV. Consequently, if one divertor leg is hotter than the other, neutrals will be preferentially ionized in the hotter divertor. Ionization source strengths would be most imbalanced near the separatrix, since these flux surfaces are accessible to neutrals in the private flux region. Reversed parallel flows driven by this effect would therefore be restricted primarily to the separatrix region and would depend mostly on the degree of temperature asymmetry in the inner and outer divertor legs. This picture is consistent with what is observed in these experiments.

8. Summary

Low-recycling (sheath-limited), high recycling, and detached divertor conditions have been investigated by direct examination of temperature and pressure gradients along magnetic field lines. A phenomenon associated with divertor detachment, termed the divertor 'death-ray', is described. Detached, high-recycling and low-recycling regimes can occur on different SOL flux surfaces in the same discharge. The spatial transition between high- and low-recycling regimes is consistent with a variation in volumetric power losses in the divertor: volumetric plus sheath heat losses combine to cause the largest parallel temperature gradients to form near the strike point.

Parallel momentum loss and subsequent divertor detachment is consistent with the Stangeby model [20] in which ion–neutral collisions remove parallel momentum in the divertor plasma. During detachment, ion–neutral collisions are found to be 10% efficient in removing parallel momentum implying that the neutral 'fluid' in the divertor acquires a toroidal velocity that approaches 90% of the plasma flow speed. The divertor 'death-ray', a highly localized increase in electron pressure at the divertor plate, may be caused by a redistribution of parallel momentum across the divertor fan via the intermediary flowing neutral fluid.

Cross-field heat transport is investigated by studying profiles of electron temperature and density in detail. All cross-field profiles display a clear non-exponential dependence on the flux surface coordinate, with the shortest gradient scale lengths appearing near the separatrix. H-mode plasmas exhibit a very short pressure gradient scale length at the separatrix (~ 1 mm) with over a factor of 10 variation across the profile.

Although the plasma density and temperature profiles exhibit complicated, non-exponential dependencies on the cross-field coordinate, it is found that the *local* pressure gradient scale length is a strong function of the *local* electron temperature in L-mode plasmas. Such a scaling is expected when parallel heat transport is dominated by classical parallel electron conduction and cross-field transport is approximately proportional to the local cross-field pressure gradient.

A surprising result is that both the density and temperature gradient scale lengths were significantly reduced when a neutral bypass leak in the divertor was closed. The implication is that cross-field heat transport in the SOL depends on the local neutral density and/or the location of the ionization sources. This result resembles core confinement observations in which the ability to access H-mode regimes depends on the control of the neutral density in the main chamber.

Another surprising result is that cross-field density and temperature gradient scale lengths are insensitive to the magnitude of toroidal field strength (B_T) for over a factor of 2.5 variation in B_T. Regression analysis performed on the local pressure gradient scale length for L-mode plasmas implies a scaling of $\chi_\perp$ with local parameters, $\chi_\perp \propto T_e^{-0.6} n^{-0.6} L^{-0.7}$.

Cross field diffusivities ($\chi_\perp$) are found to generally increase by a factor of ~ 3 over the SOL width in L-mode plasmas, consistent with the local scaling law. H-mode plasmas violate the scaling law, showing a factor of ~ 10 increase in $\chi_\perp$ over the first 3 mm of the SOL and remaining relatively flat outside this region.

$\chi_\perp$ at the separatrix is reduced from ~ 0.8 to ~ 0.25 $\mathrm{m^2\ s^{-1}}$, by improving the neutral retention characteristics of the divertor (closing neutral bypass leak). H-mode discharges show an additional drop in $\chi_\perp$ at the separatrix, down to values of ~ 0.08 $\mathrm{m^2\ s^{-1}}$. An important implication is that the H-mode transport barrier extends partially into the SOL.

Low density discharges with a hot SOL (low collisionality) exhibit a large divertor asymmetry, having outside/inside electron temperature ratios approaching ~ 10 with normal B_T and ~ 0.2 with reversed B_T. As the collisionality in the SOL increases the magnitude of the asymmetry decreases, vanishing in the highest density (lowest edge temperature) discharges.

It is shown that asymmetric parallel heat fluxes in the SOL plasma due to parallel currents can significantly contribute to the total heat flux arriving at the divertor surfaces. A large component of the parallel current is thermoelectric in nature, consistent with classical parallel electron conduction and driven by the inside/outside temperature asymmetry. A runaway situation in which thermoelectric currents cause inside/outside heat flux asymmetries was examined. This mechanism, which scales with

SOL collisionality, may be largely responsible for the observed divertor asymmetries. It is speculated that a 'seed current' driven by the toroidal loop voltage could, in principle, determine the direction of the asymmetry–hotter on the outer divertor whenever the $B \times \nabla B$ ion drift direction is towards the x-point.

The magnitude and direction of the parallel particle flows in SOL is found to depend on the inside/outside temperature asymmetry. Reversed parallel flows in the entrance to the outer divertor are routinely detected in discharges that have a hotter outer divertor. These observations suggest that the relative balance of ionization source strengths in the divertor legs influences the parallel flow profiles in the SOL. The parallel flow reversal seen at the entrance to the outer divertor may in fact be part of a large convection loop that encircles the entire core plasma.

Acknowledgements

These results were made possible by a lot of hard work and dedication from the few engineers, technical staff, students, and scientists on the Alcator team. Software support and maintenance of the edge database by Josh Stillerman and Tom Fredian is especially appreciated.This work is supported by US Department of Energy Contract No. DEAC02-78ET5 103.

References

[1] F. Wagner et al., Phys. Rev. Lett. 49 (1982) 1408.
[2] M. Greenwald et al., Phys. Rev. Lett. 53 (1984) 352.
[3] B. Tubbing et al., Nucl. Fusion 31 (1991) 839.
[4] D.M. Meade and the TFTR group, in: Plasma Physics and Controlled Nuclear Fusion Research 1990, Vol I (Proc. 13th Int. Conf., Washington DC, 1990) (IAEA, Vienna, 1991) p. 9.
[5] E.J. Strait et al., Phys. Rev. Lett. 75 (1995) 4421.
[6] I.H. Hutchinson et al., Plasma Phys. Control. Fusion 37 (1995) 1389.
[7] G.M. Staebler, submitted to Nucl. Fusion.
[8] B. LaBombard, 'Thermoelectric currents in the scrape-off layer as a mechanism to support inside/outside divertor asymmetries in Alcator C-Mod', paper in progess.
[9] P.I.H. Cooke and A.K. Prinja, Nucl. Fusion 27 (1987) 1165.
[10] C.S. Pitcher et al., in: Controlled Fusion and Plasma Physics, 1993, Vol. I, Proc. 20th Eur. Conf., Lisboa, Eur. Phys. Soc., Petit Lancy (1994) p. 291.
[11] B.L. Stansfield et al., J. Nucl. Mater. 220–222 (1995) 1121.
[12] I.H. Hutchinson et al., Phys. Plasmas 1 (1994) 1511.
[13] B. Lipschultz et al., J. Nucl. Mater. 220–222 (1995) 50.
[14] G.F. Matthews et al., Plasma Phys. Control. Fusion 32 (1990) 1301.
[15] P.C. Stangeby, in: Diagnostics, eds. O. Auciello and D. Flamm, Vol. 1 (Academic Press, Boston, MA, 1988) p. 157.
[16] R.S. Granetz et al., Rev. Sci. Instrum. 61 (1990) 2967.
[17] L.L. Lao et al., Nucl. Fusion 25 (1985) 1611.
[18] A. Niemczewski et al., submitted to Nucl. Fusion.
[19] I.H. Hutchinson et al., M.I.T. Plasma Fusion Center Report PFC/RR- 95-12 (1995).
[20] P.C. Stangeby, Nucl. Fusion 33 (1993) 1695.
[21] F. Wising et al., Contr. Plasma Phys. 36 (1996) in press.
[22] D.E. Post, J. Nucl. Mater. 220–222 (1995) 143.
[23] S.I. Krasheninnikov et al., Phys. Lett. A214 (1996) 285.
[24] A. Niemczewski, M.I.T. Plasma Fusion Center Report PFC/RR-95-8 (1995).
[25] C. Kurz, M.I.T. Plasma Fusion Center Report PFC/RR-95-5 (1995).
[26] B. LaBombard et al., Bull. Am. Phys. Soc. 40 (1995) 1703.
[27] B. LaBombard et al., Phys. Plasmas 2 (1995) 2242.
[28] K. Shimizu et al., J. Nucl. Mater. 196–198 (1992) 476.
[29] R.D. Monk et al., J. Nucl. Mater. 220–222 (1995) 612.
[30] A. Loarte, Modelling of Alcator C-Mod using the EDGE2D code (1995), private communication.
[31] S.M. Kaye et al., J. Nucl. Mater. 121 (1984) 115.
[32] S. Senguku et al., J. Nucl. Mater. 176&177 (1990) 65.
[33] G.L. Jackson et al., J. Vac. Sci. Technol. A10 (1992) 1244.
[34] P.R. Bevington, Data Reduction and Error Analysis for the Physical Sciences (McGraw-Hill, New York, 1969).
[35] A. V. Chankin et al., Plasma Phys. Control. Fusion 36 (1994) 1853.
[36] A. W. Leonard et al., J. Nucl. Mater. 220–222 (1995) 325.
[37] N. Asakura et al., J. Nucl. Mater. 220–222 (1995) 395.
[38] N. Asakura et al., Nucl. Fusion 35 (1995) 381.
[39] P. J. Harbor et al., J. Nucl. Mater. 162–164 (1989) 236.
[40] A.V. Chankin et al., J. Nucl. Mater. 196–198 (1992) 739.
[41] K. Itami et al., J. Nucl. Mater. 196–198 (1992) 757.
[42] S.I. Braginskii, in: Review of Plasma Physics, ed. M.A. Leontovich, Vol. 1 (Consultants Bureau, New York, 1965) p. 205.
[43] P.C. Stangeby, Phys. Fluids 27 (1984) 682.
[44] R.A. Langley et al., Nucl. Fusion (1994) special Issue.
[45] I.H. Hutchinson, Phys. Fluids 30 (1987) 3777.